Research Article Vol. 31, No. 24 / 20 Nov 2023 / Optics Express 39433

Optics EXPRESS

Hybrid cubic-chessboard metasurfaces for wideband angle-independent diffusive scattering and enhanced stealth

MUSTAFA K. TAHER AL-NUAIMI,[1,2,3,*] WILLIAM G. WHITTOW,[1] GUAN-LONG HUANG,[2] RUI-SEN CHEN,[2] AND QIANG SHAO[2]

[1] Wireless Communications Research Group, Loughborough University, Loughborough LE11 3TU, UK
[2] Foshan University, Foshan 528225, China
[3] State Key Laboratory of Millimeter Waves, Southeast University, China
[*] M.Al-Nuaimi@lboro.ac.uk

Abstract: Because of the shortcomings associated with their scattering patterns, both the chessboard and cubic phased metasurfaces show non-perfect diffusion and hence sub-optimal radar cross section reduction (RCSR) properties. This paper presents a novel and powerful hybrid RCSR design approach for diffusive scattering by combining the unique attributes of cubic phase and chessboard phase profiles. The hybrid phase distribution is achieved by simultaneously imposing two distinct phase profiles (chessboard and cubic) on the hybrid metasurface area with the aid of geometric phase theory to further enhance the diffusive scattering and RCSR. It is shown in this paper that through the integration of cubic and chessboard phase profiles, a metasurface with the hybrid phase mask successfully overcomes all the above issues and shortcomings related to the RCSR of both chessboard and cubic metasurfaces. In addition, the proposed design leverages the unique scattering properties offered by these distinct phase profiles to achieve enhanced stealth capabilities over wide frequency ranges and for large incidence angles. Simulation and measurement results show that the designed hybrid metasurfaces using the proposed strategy achieved RCSR and low-level diffused scattering patterns from 12–28 GHz (80%) for normal incidence of a far-field CP radar plane wave. The hybrid metasurface shows a stable angular diffusion and RCSR performance when the azimuthal and elevation incidence angles are in the range of $0° \rightarrow \pm 75°$ which is wider than other designs in the literature. Therefore, this work can make objects significantly less detectable in complex radar environments when enhanced stealth is required.

1. Introduction

Modern stealth technology demands innovative material solutions to effectively minimize the backscattering and maximize the radar-cross-section reduction (RCSR) of various objects [1]. Achieving effective stealth capabilities, minimizing the detectability of objects, and enhancing their performance in radar environments are crucial challenges in domains ranging from defense and aerospace to telecommunications and remote sensing. Traditional methods for stealth and RCSR often focus on altering the shape of objects or incorporating radar-absorbing materials, but these approaches have limitations, especially when considering complex geometries and diverse incident angles [2–4]. Metasurfaces, a class of artificially engineered surfaces with subwavelength meta-atoms, have emerged as a revolutionary technology with the potential to manipulate the EM wave properties such as phase, amplitude, and polarization [5–9]. While metasurface have gained significant attention for their capabilities in creating lenses [10–12],

#504200 https://doi.org/10.1364/OE.504200
Journal © 2023 Received 25 Aug 2023; revised 26 Oct 2023; accepted 26 Oct 2023; published 6 Nov 2023

Optics EXPRESS

beam steering [13], and frequency-selective surfaces [14], their potential for diffusion and RCSR, especially at oblique and non-specular angles, remains a promising and current research topic.

Inspired by the alternating pattern of colors on a chessboard, metasurfaces with a configuration of two-phase states (i.e., 0° and 180°) have been designed in the literature and called chessboard metasurfaces to effectively reduce the monostatic RCS under normal incidence [15–17]. The most important advantage of such chessboard configurations is that a properly designed chessboard metasurface can be engineered to operate across a wide range of radar frequencies, leading to broadband monostatic RCSR in the boresight direction. While a chessboard metasurface has unique potential for reflection suppression in the boresight direction, it also has certain limitations and potential shortcomings in terms of scattering patterns, polarization sensitivity, and response under oblique incidence. The RCSR performance of a chessboard metasurface is polarization sensitive [18]. The scattering pattern effectiveness may vary with the polarization of the incident radar EM wave, potentially limiting the RCSR capabilities as the polarization of the incoming wave is unknown in real world applications [19]. Chessboard metasurfaces may not be the best option for oblique incidence angles as the RCSR of such metasurfaces deteriorates significantly for off-normal angles of incidence. In addition, chessboard metasurfaces produce a scattering pattern with four lobes of strong diffraction in some directions which limits their use for bistatic RCSR. Thus, digital coding metasurfaces were proposed in the literature and successfully overcame these limitations associated with the chessboard metasurface approach [20–23]. However, these coding metasurfaces have a complicated design challenge related to finding the optimum 1-bit, 2-bit, or even 3-bit random phase distribution for significant RCSR. This requires the use of various optimization techniques and repeated numerical simulations to reach the optimum random coding sequence and to evaluate the scattering and EM responses of the random coding metasurfaces. For instance, this step involves refining the phase distribution iteratively based on the desired diffusion objectives, which is a lengthy process and needs a huge computational resource. The lack of an easy-to-solve phase design formula makes the coding metasurface design hard to be reproduced by other researchers. Recently a cubic phase profile metasurface, for accelerated beam generation, is a novel concept that combines the advanced beam-shaping capabilities of a cubic phase metasurface with the concept of beam acceleration [24–27]. The cubic phase profile can be designed to achieve complex beam shaping, including creating highly focused beams, generating customized wave patterns, or steering beams in specific directions [28,29].

In this context, this paper aims to delve into the application of hybrid metasurface for both diffusion control and RCSR of a metallic plate under wide incident angles. An innovative design strategy based on the combination and integration of two distinct phase profiles (chessboard and cubic) are used to achieve a hybrid phase mask that overcomes all limitation associated with the chessboard, cubic, and random coding metasurfaces. The presented hybrid metasurface has a design formula for the phase calculation which ensures RCSR > 10 dB from 12–28 GHz (80%) and maximum incident angles in both azimuthal and elevation planes of ±75°.

2. Reflective geometric phase meta-atom design

In this section, the design and simulation methodology for the individual meta-atom that compose the hybrid metasurface is presented employing the CST Microwave Studio software as the simulation tool. Meta-atoms serve as the fundamental building blocks of the metasurface structure. Alongside the phase distribution across the metasurface aperture, the properties of these meta-atoms play a pivotal role in shaping the overall electromagnetic response of the hybrid metasurface. The structure of the meta-atom used in this paper is depicted in Fig. 1, whose periodicity $P = 4.8$ mm. The designed meta-atom is composed of a copper strip patterned on the topside of a dielectric board (RO4003C, thickness $h = 2.03$ mm and $\varepsilon_r = 2.2$) and backed with solid copper ground plane layer. The thickness of the copper layers of the meta-atom is 18 μm and

Optics EXPRESS

the optimized physical dimensions of the meta-atom are $L = 1.4$ mm, $S = 0.4$ mm, $M = 1.3$ mm, and $N = 0.2$ mm. The simulated reflection characteristics (amplitude and phase) of the meta-atom were computed using CST Microwave Studio software with Floquet ports and periodic boundary conditions as shown in Fig. 1. A graph displaying the amplitudes (cross-pol and co-pol) of the meta-atom's reflection coefficients is depicted in Fig. 1(b). When exposed to a CP incident plane wave, the meta-atom's unique anisotropic geometry leads to three distinct resonances (according to Faraday's law) in the meta-atom's reflection characteristics that result in varying phase shifts, influencing its interaction with incident electromagnetic waves at 15.2, 18.1, and 24.3 GHz as shown in Fig. 1(b). The anisotropic meta-atom exhibits strong co-polarized (co-pol) reflection response close to 0 dB, while maintaining low cross-polarized (cross-pol) reflection of less than −18 dB from 12.8 GHz to 26 GHz. The plot in Fig. 1(c) illustrates the change in the geometric reflection phase ($\phi_{Geometric}$) of the co-pol reflection component of the meta-atom as it undergoes rotation. The graph showcases how altering the meta-atom's orientation angle (ψ) results in a dynamic shift in the reflected phase of the co-pol component which cover the 360° phase range required for efficient manipulation of EM wave diffusion and hence RCSR. It is worth mentioning that the meta-atom satisfies the geometric phase requirements and $\phi_{Geometric} = \pm 2\psi$ and therefore, any phase compensation value between 0° and 360° on the metasurface area can be achieved by rotating the meta-atom to the desired angle [30].

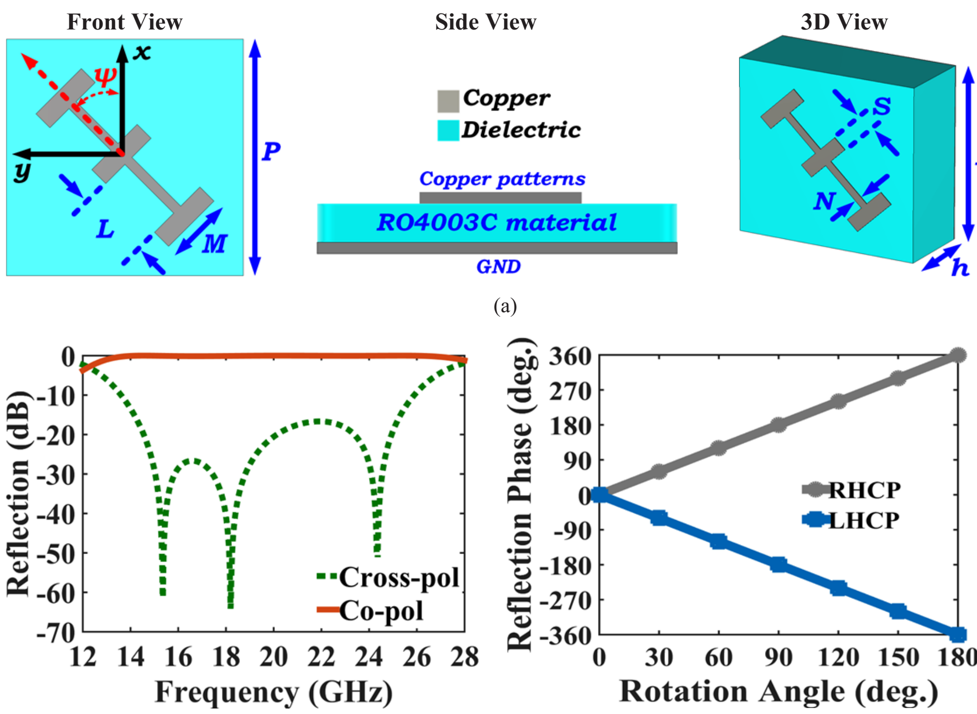

(a)

(b) (c)

Fig. 1. (a) Front, side, and 3D views of the reflective geometric phase meta-atom. (b) A graph depicting the simulated amplitudes of the meta-atom's reflection coefficients as functions of frequency with a CP plane wave normally impinging on the meta-atom. (c) Plot illustrating the simulated geometric reflection phase response of the meta-atom as a function of the meta-atom rotation angle (ψ) varying from 0° to 180°.

Optics EXPRESS

3. Hybrid metasurface design and results

The concept of combining cubic and chessboard phase profiles in a single metasurface aims to capitalize on their complementary scattering behaviors and to overcome all issues related to their RCSR shortcomings as shown in Fig. 2. The cubic phase introduces gradual phase shifts across the metasurface, resulting in controlled redirection of incident waves [31–33]. On the other hand, the chessboard phase profile alternates between two discrete phase values (0° and 180°), contributing to the mitigation of specular reflections. This innovative hybrid approach aims to achieve enhanced RCSR capabilities and more uniformly diffused scattering patterns through the cooperative effects of these two distinct phase manipulation techniques. Cubic, chessboard, and hybrid metasurfaces composed of 40×40 meta-atoms and occupying a volumetric size of $192 \times 192 \times 2.03$ mm^3 were designed and their diffusion and RCSR performance was evaluated using CST Microwave Studio. Three phase profiles, namely cubic phase (ϕ_{Cubic}), chessboard phase (ϕ_{Chess}), and hybrid phase (ϕ_{Hybrid}), have been calculated using Eqs. (1), (2), and (3)

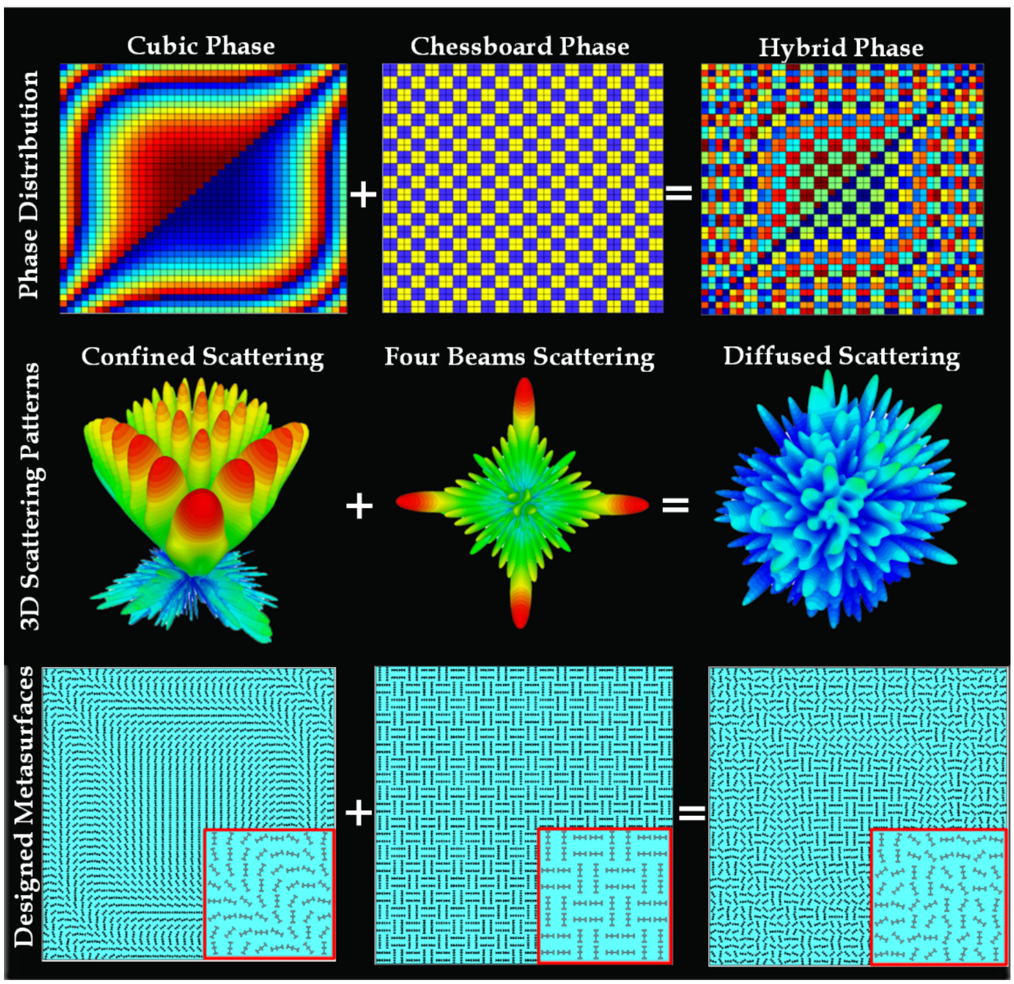

Fig. 2. Calculated cubic, chessboard, and hybrid phase profiles (top row) and their typical 3D scattering patterns (middle row), and the three designed metasurfaces (bottom row) with 5× magnification inset images. All metasurfaces contains 40×40 meta-atoms and the maximum linear dimension is $D = 192$ mm.

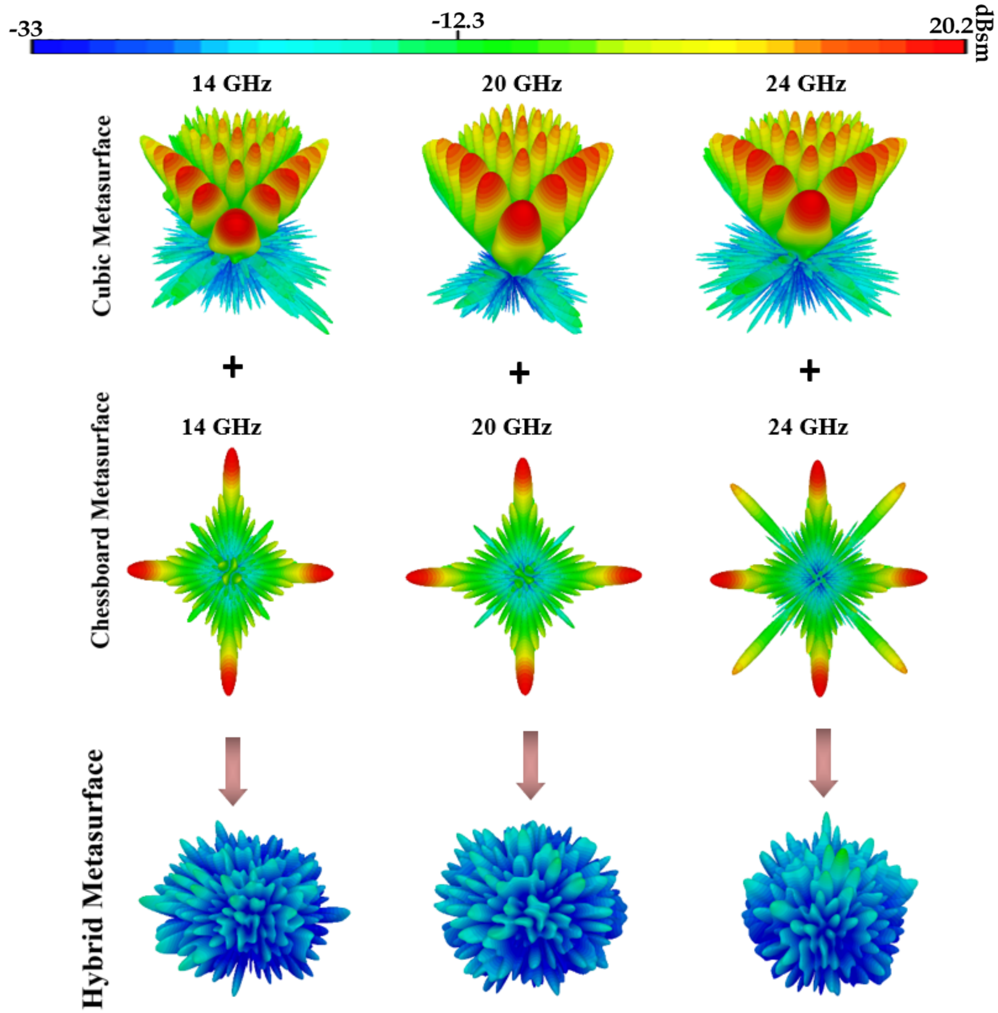

Fig. 3. Simulated 3D scattering patterns of the cubic, chessboard, and hybrid metasurfaces when normally exposed to a far-field CP plane waves at various frequencies.

[24–29]. In these formulas, x_c and y_c represent the coordinates of the meta-atom in the xy-plane, $\alpha = 25$ is the phase shift constant of the ideal cubic phase, and $D = 192$ mm is the maximum linear dimension of the three metasurfaces.

$$\phi_{Cubic}\left(x_c, y_c\right) = \frac{\alpha}{D^3}(x_c^3 + y_c^3) \tag{1}$$

$$\phi_{Chess}\left(x_c, y_c\right) = 0^o \ or \ 180^\circ \tag{2}$$

$$\phi_{Hybrid}\left(x_c, y_c\right) = \phi_{Chess}\left(x_c, y_c\right) + \ \phi_{Cubic}\left(x_c, y_c\right) \tag{3}$$

The calculated phase profiles calculated based on Eqs. (1), (2), and (3) are shown in Fig. 2 (top row). As can be seen in Fig. 2 (top row), the 2D cubic phase profile is asymmetric and varies cubically across the metasurface in the xy-plane. This introduces a more complex phase distribution compared to linear or quadratic phase profiles. Asymmetrical phase profiles can lead to unconventional wavefront shaping and scattering behavior. By introducing variations in the phase that do not exhibit symmetry, one can create more complex scattering patterns and

Optics EXPRESS

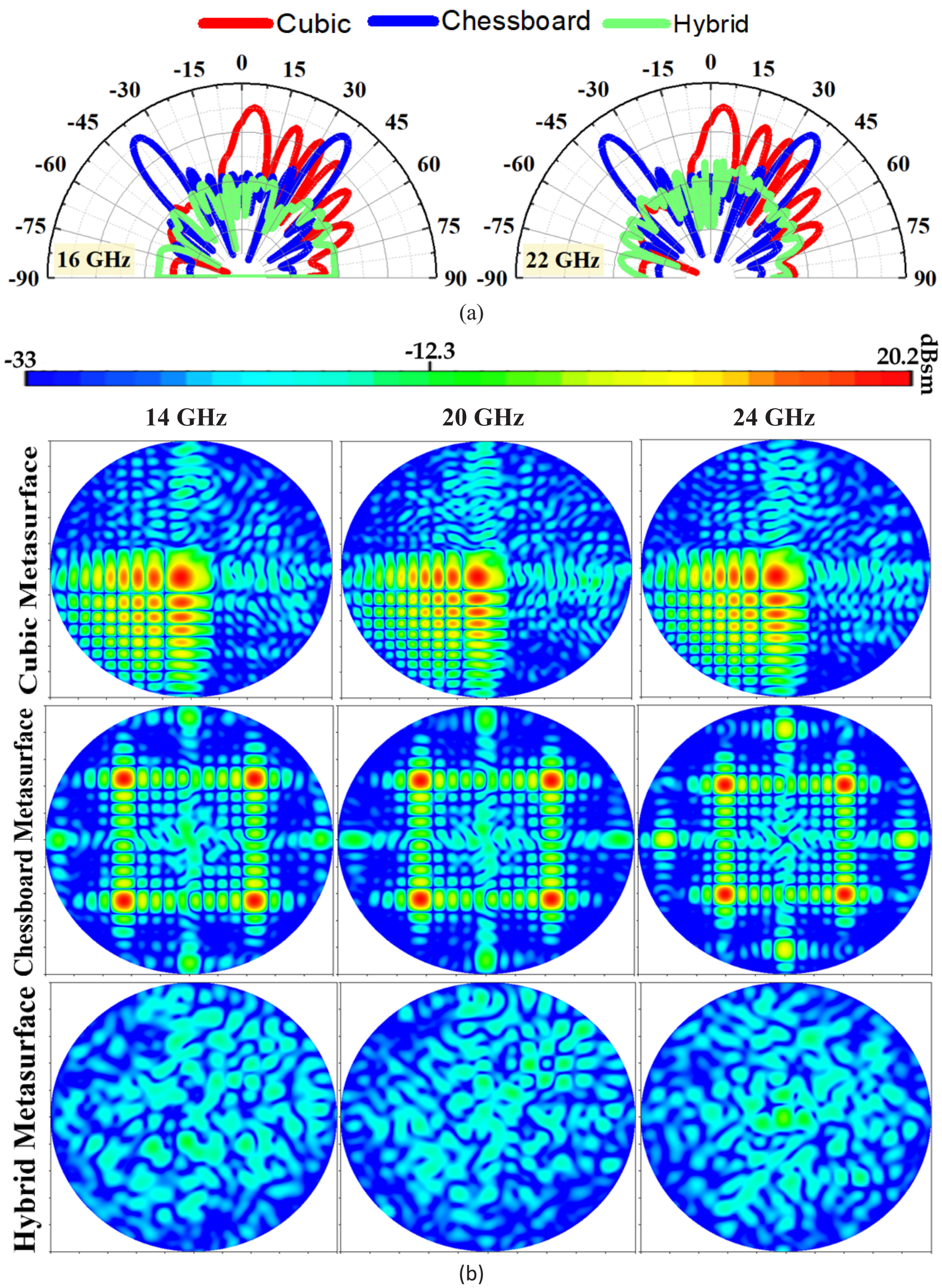

Fig. 4. (a) Simulated 2D polar plots of the far-field scattering patterns of the three metasurfaces. (b) Simulated backscattered energy distribution in front of the three metasurfaces at 14, 20, and 24 GHz.

finely control the distribution of scattered energy in different directions. On the other hand, the phase profile of a chessboard metasurface phase profile in Fig. 2 (top row) with a 180° phase shift alternates between two discrete phase values, typically 0° and 180°, across the metasurface.

Optics EXPRESS

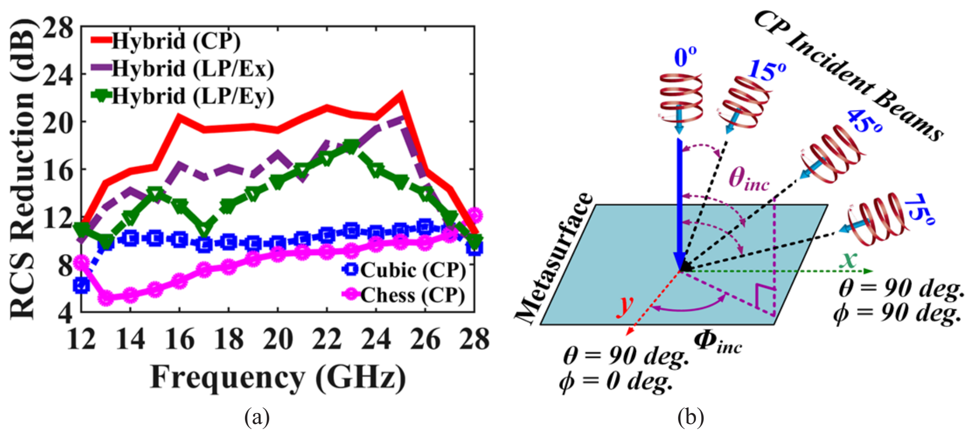

Fig. 5. (a) Simulated RCS reduction curves of the three metasurfaces under normal incidence. (b) Plot illustrating the incident azimuthal and elevation angles used in this paper.

In a chessboard metasurface phase profile, the adjacent meta-atoms are assigned different phase values, resulting in a chessboard-like pattern. The hybrid phase profile is a combination of the cubic and chessboard phase profiles as shown in Fig. 2 (top row). The 3D scattering patterns of the three phase profiles are presented in in Fig. 2 (middle row). Based on the three phase profiles, three metasurfaces have been designed using the anisotropic meta-atom in the previous section as shown in Fig. 2 (bottom row). A MATLAB code was used to automatically control the CST Microwave Studio to construct the three metasurfaces and to compute the scattering patterns. The backscattering performances of the cubic, chessboard, and hybrid metasurfaces were investigated using the T-solver of the CST Microwave Studio by computing the 3D scattering patterns as shown in Fig. 3. For the metasurface with cubic phase profile (top row in Fig. 3), the incident CP plane wave was backscattered and reflected as a group of focused beams in certain directions without being severely diffused.

The beams have been concentrated next to each other in a small angular angle, and hence the magnitude of the reflected patterns is significant. For the chessboard metasurface (middle row in Fig. 3), the backscattering in the boresight direction has been significantly reduced as can be seen at the center of the scattering patterns. However, the scattering patterns of the chessboard metasurface contains four lobes of strong scattering and these strong scattering lobes limit its use for stealth applications as it will be detected easily by the bistatic radar. To conclude, the scattering patterns of both cubic and chessboard metasurfaces are not perfect for stealth applications as it will be detected easily by the bistatic radar. For the hybrid metasurface design that incorporates both continuous (cubic phase) and discrete (chessboard phase) phase profiles on the same metasurface, the scattering patterns are displayed in Fig. 3 (bottom row). As shown the resulted scattering patterns from the combination of two distinct phase profiles are totally different from those of the cubic and chessboard metasurfaces. It can be seen in Fig. 3 (bottom row) that the hybrid scattering patterns are significantly diffused in countless directions and uniformly distributed in the half-plane in front of the hybrid metasurface. It has been noticed that the strong scattering lobes of the cubic and chessboard scattering patterns have been suppressed and the hybrid scattering pattern does not have strong scattering in any direction and the hybrid metasurface design can indeed lead to improved scattering patterns that are more uniform and well-distributed. This is because the hybrid approach takes advantages of both distinct phase profiles. For further understanding of the advantages of the hybrid approach, the 2D polar plots at 16 and 22 GHz show how the magnitude of the scattered waves is distributed across different angles in a circular fashion as shown in Fig. 4(a). When compared to cubic

Optics EXPRESS

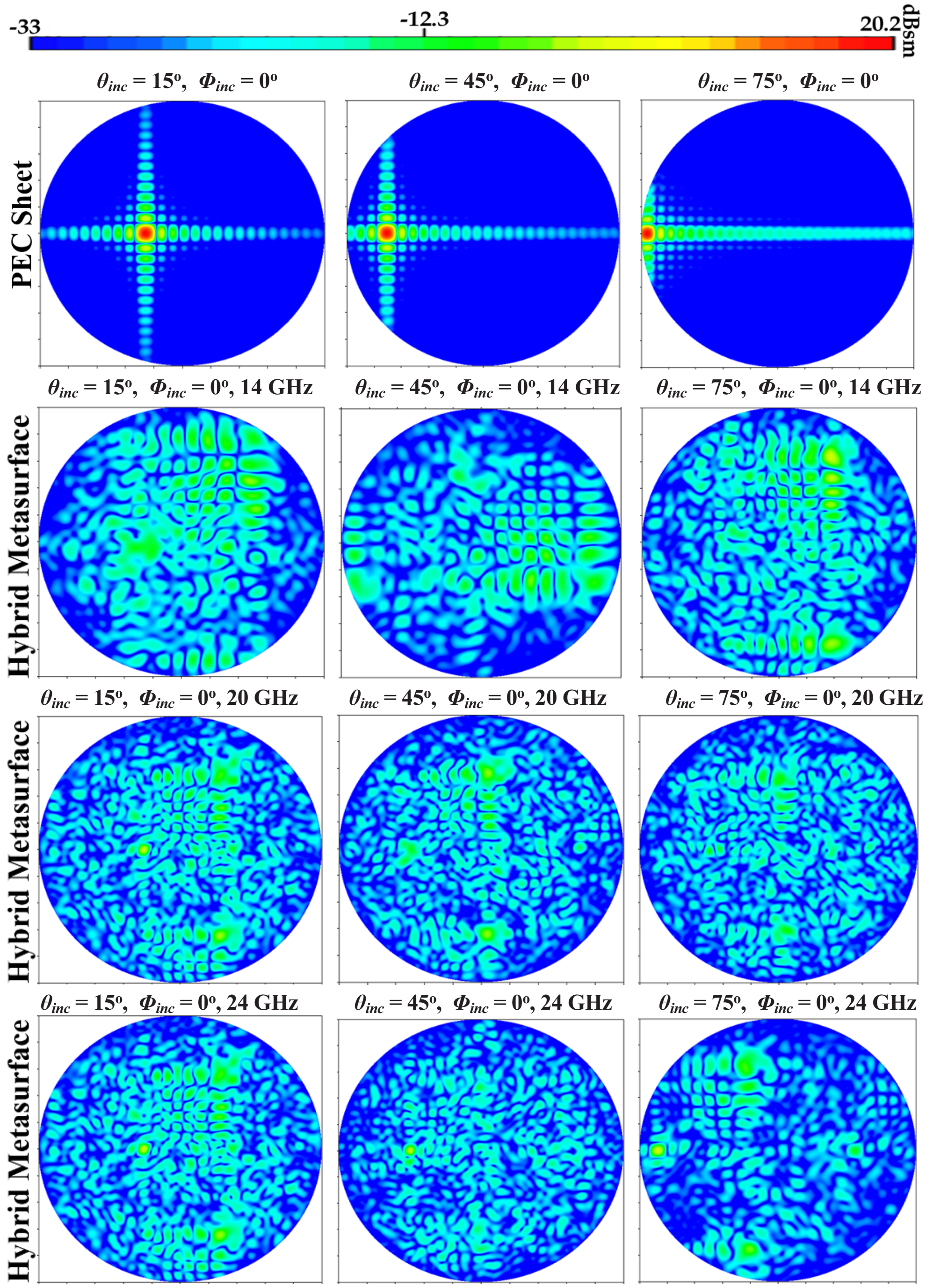

Fig. 6. Simulated backscattered energy distribution of the hybrid phased metasurface under oblique incidence of a far-field plane wave for $\theta_{inc} = 15°$, 45°, and 75° with $\Phi_{inc} = 0°$.

and chessboard scattering patterns, the hybrid scattering patterns show a lower scattering in all directions with suppression of strong scattering lobes. To further emphasize the ability of the hybrid technique in RCSR, the 2D backscattered energy distribution of the cubic, chessboard,

Optics EXPRESS

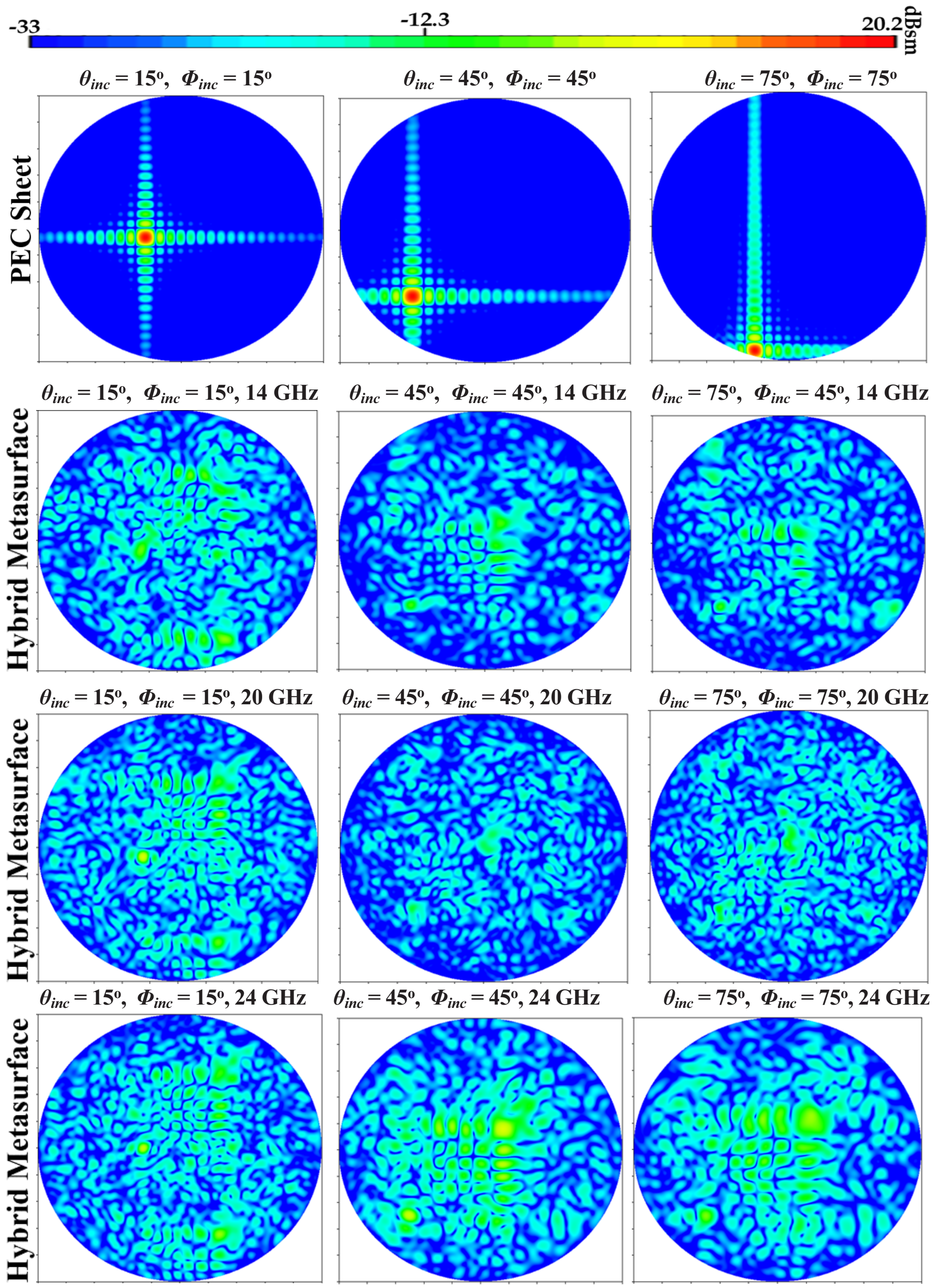

Fig. 7. Simulated backscattered energy distribution of the hybrid phased metasurface under oblique incidence of far-field plane waves with a range of incidence angles: $\theta_{inc} = 15°$, 45°, and 75° with $\Phi_{inc} = 15°$, 45°, and 75°.

and hybrid metasurfaces have been computed at various frequencies using CST Microwave Studio and the results are shown in Fig. 4(b). It can be seen that for the cubic metasurface, the far-field scattering patterns with several lobes concentrated in the third quadrant (lower left portion) of the angular space, which is a common characteristic of cubic phase metasurfaces and other diffractive optical elements. These lobes are essentially regions of enhanced scattering intensity that are distributed around the central direction of reflection. A scattering pattern with four lobes concentrated along the diagonal directions typically indicates a typical behavior of a chessboard metasurface. The presence of four lobes in the diagonal directions of the scattering pattern suggests that the design of the chessboard metasurface is causing incident waves to scatter predominantly in these diagonal angles. For the hybrid metasurface, the backscattered energy has been well diffused and distributed over all angles which results in a significant RCSR. The RCSR performance of the three metasurfaces was computed using CST Microwave studio from 12 to 28 GHz when three metasurfaces were normally exposed to far-field CP and LP plane waves as shown in Fig. 5(a). The RCSR of the chessboard metasurface is less than 10 dB, while the RCSR of the cubic metasurface fluctuates around the 10 dB level. The hybrid metasurface significantly reduced the the RCS from 12–28 GHz for normal incidence of a far-field CP and LP radar plane wave which confirms that the hybrid technique is very powerful for RCSR and insensitive to polarization of the incoming wave. The RCSR, diffusion performance, and angular stability of the hybrid metasurface was further investigated under off-normal incidence (the angles are shown in Fig. 5(b)) of far-field CP plane wave as shown in Fig. 6 when the azimuthal $\Phi_{inc} = 0°$ and elevation (θ_{inc}) incidence angle were varied from 15° to 75°. While in Fig. 7, both azimuthal angles Φ_{inc} and θ_{inc} were varied from 15° to 75°.

As can be seen in Fig. 6 and Fig. 7, the hybrid metasurface show a wide and stable angular stability for Φ_{inc} and θ_{inc} <75°. It is worth noting that the bottom row in Fig. 7 shows the RCS reduction performance at both the frequencies at the edge and the widest angle of incidence. As observed in the literature, metasurfaces often exhibit different radiation patterns at different frequencies, but as long as the RCS reduction remains consistently above 10 dB, the results can be deemed acceptable. It can be seen that the hybrid metasurface has a very stable RCSR and diffusion characteristics under off-normal incidence of far-field CP plane wave and maintain this significant RCSR behavior from 12–28 GHz. RCSR of an object under oblique incidence is very necessary in real world applications where bistatic radar may be used.

4. Fabrication and experimental validation

To validate the hybrid design approach and experimentally verify the RCSR results of the hybrid metasurface, a prototype was fabricated using the low-cost printed circuit board (PCB) technology, see Fig. 8(a). The overall dimensions of the fabricated hybrid metasurface are $192 \times 192 \times 2.03$ mm^3. A representative sketch of the reflection measurement setup is shown in Fig. 9(b), in which two identical horn antennas operating from 10–30 GHz were utilized as a transmitter (Tx horn) and receiver (Rx horn). The horn antennas were connected the ports of network analyzer. The reflection from a copper sheet was measured as well and used as a reference for RCS measurements. The horn antennas and the metasurface under test were placed on the same height and carefully aligned using laser distance meter (Leica DISTO X3-1). The distance R between the horn antennas and the metasurface undertest inside the anechoic chamber was chosen carefully based on the far-field formula ($R > 2D^2/\lambda$). With D = 192 mm and $\lambda = 25$ mm at 12 GHz, R should be greater than 2.9 m, in our paper R was chosen as 3 m. A photograph shows the measurement setup inside the anechoic chamber is presented in Fig. 8(c). The measured and simulated RCSR versus frequency results are depicted in Fig. 8(d). The RCSR is greater than 10 dB from 10 to 28 GHz which confirms the simulation results presented in the previous section. While our simulated and measured RCSR data demonstrates a commendable level of consistency, it is essential to acknowledge a slight disparity between the simulated and measured

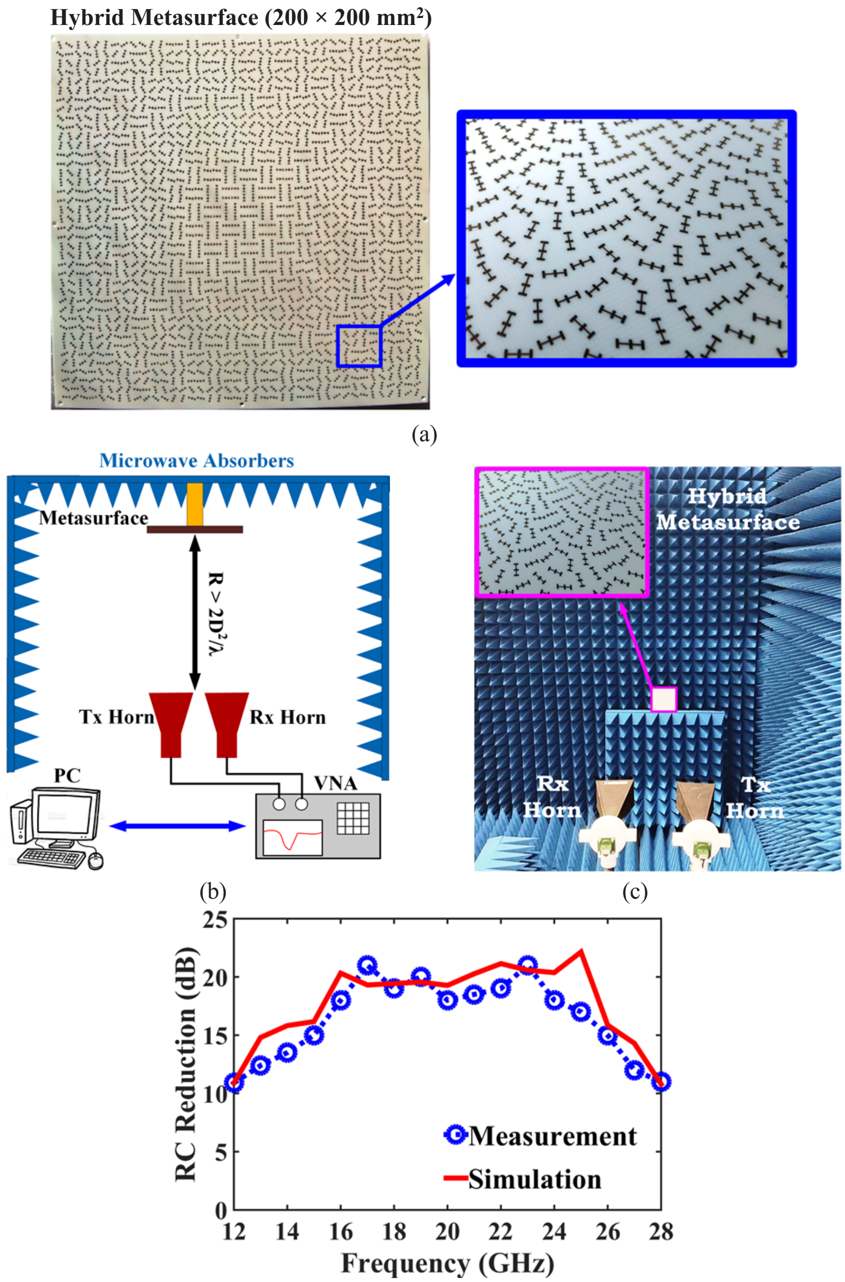

Fig. 8. (a) Photograph of the fabricated hybrid metasurface. (b) A sketch illustrating the reflection measurement setup. (c) Photograph of the reflection measurement setup inside the anechoic chamber. (d) The measured and simulated RCSR curve versus frequency.

results. This disparity may be attributed to a combination of factors, including uncertainties associated with the dielectric constant of the substrate within the operating frequency band, potential misalignments between the horn antennas and the metasurface during testing within the anechoic chamber, as well as variations stemming from the fabrication process, including errors and tolerances.

To elucidate the diffusion and RCSR performance of the hybrid metasurface, comparison study was conducted to further emphasize the effectiveness of the hybrid metasurface over other design approaches in the literature as shown in Table 1. It is noticed that the 10 dB RCSR bandwidth of the hybrid metasurface exceeds most of those metasurfaces in the literature that were designed using various approaches. In addition, the hybrid metasurface achieved more than 10 dB of RCSR with a fractional bandwidth of 80% under both normal and oblique incidences To have a fair comparison, angular stability for more than 10 dB of RCSR was also compared and as can be seen in Table 1, the hybrid metasurface maintained a stable diffusion and RCSR performance for angles up to 75° which is wider than other designs in the literature. In summary, the comparison table indicates that the hybrid metasurface achieves wideband RCSR while also maintaining excellent angular stability. In the proposed design strategy, the RCS reduction performance observed under both normal and oblique incidence angles is a direct outcome of the interplay between the meta-atom characteristics and the hybrid phase distribution.

Table 1. Performances of the hybrid metasurface in comparison to previous works[a]

Ref.	RCSR Mechanism	Periodicity (λ_c)	Thickness (mm)	10 dB RCSR BW (GHz)	10 dB RCSR FBW (%)	Angular stability >10 dB RCSR θ_{inc}, Φ_{inc}
[30]	Diffusion	0.48	2.0	12–23	62.9	N.A., N.A.
[34]	Absorption	0.34	2.0	12.3-28.4	78.7	N.A., N.A.
[35]	Absorption	0.14	3.5	3.8-6.8	56.6	45°, N.A.
[36]	Spiral Coded	0.36	2.0	12.2 -23.4	63.0	60°, N.A.
[37]	Diffusion	0.36	1.2	21–38	57.6	45°, N.A.
[38]	Chessboard	0.24	1.27	14.5-21.8	40.2	40°, N.A.
[39]	Chessboard	0.21	2.0	6.9-9.2	28.3	40°, N.A.
[40]	Aperiodic	0.33	2.0	9.3-15.5	50.0	30°, N.A.
[41]	Hybrid	0.34	3.23	6.7-19.4	97.9	60°, N.A.
[42]	Hybrid	0.43	4.01	11.0-15.5	34.0	30°, N.A.
[43]	Hybrid	0.42	2.65	7.5-15.2	76.7	30°, N.A.
This Work	**Hybrid**	**0.32**	**2.03**	**12–28**	**80.0**	**75°, 75°**

[a]Ref.: Reference, mm: millimeter, (λ_c): free space wavelength at the centre frequency, BW: bandwidth.

It is worth mentioning that the availability of a design formula for the hybrid phase calculation will enhance the design speed by avoiding the requirement of lengthy optimization algorithms. The proposed design is topical with the increased interest in engineered surfaces and metasurfaces for EM-wave manipulation [44–53].

5. Conclusion

In summary, a novel hybrid design approach that incorporates the cubic and chessboard phase profiles to achieve significant RCSR and enhanced stealth. The RCS reduction principle of the hybrid technique is analysed, and the related design formulas are presented. The simulated and measured results indicate that when the presented hybrid metasurface was illuminated by a CP plane wave, more than 10 dB of RCSR reduction was achieved in the frequency band from 12 to 28 GHz, with the fractional bandwidth is 80%. In addition, the wideband RCSR performance is maintained under oblique (off-normal) incidence until the azimuthal and elevation incident angles increase to 75°, which confirms the excellent angular stability of the hybrid metasurface.

The proposed hybrid design approach overcomes the shortcomings related to the scattering patterns of the cubic and chessboard metasurfaces. Furthermore, the hybrid metasurface has a reduced sensitivity to the angle of incidence which provides more design freedom to develop low backscattering metasurfaces stealth scenarios. In the proposed design strategy, the RCS reduction performance observed under both normal and oblique incidence angles is a direct outcome of the interplay between the meta-atom characteristics and the hybrid phase distribution.

Funding. Engineering and Physical Sciences Research Council ('ANISAT' EPSRC-S030301/1); Newton International Fellowship (NIF\R1\222093); State Key Laboratory of Millimeter Waves, Southeast University, China (K202317).

Disclosures. The authors declare no conflicts of interest.

Data availability. Data underlying the results presented in this paper are not publicly available at this time but may be obtained from the authors upon reasonable request.

References

1. H. Tao, N. I. Landy, C. M. Bingham, X. Zhang, R. D. Averitt, and W. J. Padilla, "A metamaterial absorber for the terahertz regime: design, fabrication and characterization," Opt. Express **16**(10), 7181–7188 (2008).
2. L. Zhang, X. Q. Chen, S. Liu, Q. Zhang, J. Zhao, J. Y. Dai, G. D. Bai, X. Wan, Q. Cheng, G. Castaldi, V. Galdi, and T. J. Cui, "Space-time-coding digital metasurfaces," Nat. Commun. **9**(1), 4334 (2018).
3. M. K. T. Al-Nuaimi, W. G. Whittow, G. -L. Huang, R. -S. Chen, and S. -W. Wong, "Wideband Radar-Cross-Section Reduction Using Parabolic Phased Metasurfaces," Antennas Wirel. Propag. Lett. **22**(7), 1547–1551 (2023).
4. A. Y. Modi, C. A. Balanis, C. R. Birtcher, and H. N. Shaman, "A New class of RCS-reduction metasurface based on scattering cancellation using array theory," IEEE Trans. Antennas Propagat. **67**(1), 298–308 (2019).
5. C. Fan, K. Duan, K. Chen, *et al.*, "Actively tunable rasorber with broadband RCS reduction and low infrared emissivity," Opt. Express **31**(14), 23294 (2023).
6. M. Feng, Y. Li, Q. Zheng, J. Zhang, Y. Han, J. Wang, H. Chen, S. Sai, H. Ma, and S. Qu, "Two-dimensional coding phase gradient metasurface for RCS reduction," J. Phys. D: Appl. Phys. **51**(37), 375103 (2018).
7. M. K. T. Al-Nuaimi, William G. Whittow, G. L. Huang, *et al.*, "Exploring the EM-Wave Diffusion Capabilities of Axicon Coding Metasurfaces for Stealth Applications," Opt. Express **31**(23), 37495–37506 (2023).
8. M. Moccia, S. Liu, R. Y. Wu, G. Castaldi, A. Andreone, T. J. Cui, and V. Galdi, "Coding metasurfaces for diffuse scattering: Scaling laws, bounds, and suboptimal design," Adv. Opt. Mater. **5**(19), e1700455 (2017).
9. Y. Xi, W. Jiang, K. Wei, T. Hong, and S. Gong, "An Optically Transparent Hybrid Mechanism Metasurface for Wideband, Wide-Angle and Omnidirectional Scattering Suppression," IEEE Trans. Antennas Propagat. **71**(1), 422–432 (2023).
10. M. K. T. Al-Nuaimi and W. Hong, "Phase Error Analysis of Discrete Dielectric Lens with Experimental Results at 94 GHz," IEEE Trans. Antennas Propagat. **63**(10), 4400–4407 (2015).
11. X. Wu and W. Zhu, "Modified metasurface Alvarez lens based on the phase compensation in a microwave band," Opt. Express **30**(14), 25400–25409 (2022).
12. M. K. T. Al-Nuaimi and W. Hong, "Discrete Dielectric Reflectarray and Lens for E-Band with Different Feed," Antennas Wirel. Propag. Lett. **13**, 947–950 (2014).
13. G. Zhou, S.W. Qu, B. Chen, *et al.*, "Metasurface-based Fourier lens fed by compact plasmonic optical antennas for wide-angle beam steering," Opt. Express **30**(12), 21918–21930 (2022).
14. X. Wang, K. Shi, J. Wang, *et al.*, "Flexible strain sensor based on a frequency selective surface," Opt. Express **31**(5), 8884–8896 (2023).
15. M. Mighani and G. Dadashzadeh, "Broadband RCS reduction using a novel double layer chessboard AMC surface," Electron. Lett. **52**(14), 1253–1255 (2016).
16. M. K. T. Al-Nuaimi, W. Hong, and Y. He, "Design of Diffusive Modified Chessboard Metasurface," Antennas Wirel. Propag. Lett. **18**(8), 1621–1625 (2019).
17. K. Li, Y. Liu, Y. Jia, and Y. J. Guo, "A Circularly Polarized High-Gain Antenna with Low RCS Over a Wideband Using Chessboard Polarization Conversion Metasurfaces," IEEE Trans. Antennas Propagat. **65**(8), 4288–4292 (2017).
18. Y. Xi, W. Jiang, T. Hong, *et al.*, "Wideband and wide-angle radar cross section reduction using a hybrid mechanism metasurface," Opt. Express **29**(14), 22427–22441 (2021).
19. H. X. Xu, S. Ma, X. Ling, *et al.*, "Deterministic Approach to Achieve Broadband Polarization-Independent Diffusive Scatterings Based on Metasurfaces," ACS Photonics **5**(5), 1691–1702 (2018).
20. M. K. T. Al-Nuaimi, G. L. Huang, W. G. Whittow, *et al.*, "Coding Engineered Reflector for Wide-Band RCS Reduction Under Wide Angle of Incidence," IEEE Trans. Antennas Propagat. **70**(10), 9947–9952 (2022).
21. T. J. Cui, M. Q. Qi, X. Wan, J. Zhao, and Q. Cheng, "Coding Metamaterials, Digital Metamaterials and Programmable Metamaterials," Light: Science and Applications **3**(10), e218 (2014).
22. Y. Zheng, X. Cao, J. Gao, *et al.*, "Shared Aperture Metasurface with Ultra-Wideband and Wide-Angle Low-Scattering Performance," Optical Materials Express **7**(8), 2706–2714 (2017).
23. M. K. T. Al-Nuaimi, G. -L. Huang, W. G. Whittow, R. -S. Chen, and S. -W. Wong, "Realization of Single Layer Fourier Phased Metasurfaces for Wideband RCS Reduction," Antennas Wirel. Propag. Lett. **22**(5), 1179–1183 (2023).

24. Z. Cai, X. Qi, D. Pan, *et al.*, "Dynamic Airy imaging through high-efficiency broadband phase microelements by femtosecond laser direct writing," Photonics Research **8**(6), 875–881 (2020).
25. B. Y. Wei, P. Chen, W. Hu, *et al.*, "Polarization-controllable Airy beams generated via a photoaligned director-variant liquid crystal mask," Sci. Rep. **5**(1), 17484 (2015).
26. Z. Wu, D. Zhu, Y. Jiang, *et al.*, "Propagation properties of hollow rectangular quad-Airy beams," Optik **272**, 170289 (2023).
27. Z. X. Fang, Y. X. Ren, L. Gong, *et al.*, "Shaping symmetric Airy beam through binary amplitude modulation for ultralong needle focus," J. Appl. Phys. **118**(20), 203102 (2015).
28. J. Wen, L. Chen, B. Yu, *et al.*, "All-Dielectric Synthetic-Phase Metasurfaces Generating Practical Airy Beams," ACS Nano **15**(1), 1030–1038 (2021).
29. P. Vaveliuk, P. Vaveliuk, A. Lencina, *et al.*, "Symmetric Airy beams," Optics Letters **39**(8), 2370–2373 (2014).
30. K. Chen, Y. Feng, Z. Yang, *et al.*, "Geometric phase coded metasurface: from polarization dependent directive electromagnetic wave scattering to diffusion-like scattering," Scientific Reports **6**(1), 35968 (2016).
31. Z. Cai, Y. Liu, C. Zhang, *et al.*, "Continuous cubic phase microplates for generating high-quality Airy beams with strong deflection," Optics Letters **42**(13), 2483–2486 (2017).
32. H. Zhao, J. Lin, J. Tan, *et al.*, "Multi-focus of modulated polarized Airy beam," Optics & Laser Technology **81**, 107–114 (2016).
33. H.Y. Kuo, S. Vyas, C. H. Chu, *et al.*, "Cubic-Phase Metasurface for Three-Dimensional Optical Manipulation," Nanomaterials **11**(7), 1730 (2021).
34. M. Feng, X. Chen, Y. Li, Q. Zheng, Y. Han, J. Zhang, J. Wang, Y. Hou, Z. Liu, X. Li, C. Wang, J. Jing, H. Ma, and S. Qu, "Circularly Polarized Spin-Selectivity Absorbing Coding Phase Gradient Metasurface for RCS Reduction," Adv. Theory Simul. **3**(3), 1900217 (2020).
35. Z. Meng, C. Tian, C. Xu, J. Wang, X. Li, S. Huang, Q. Fan, and S. Qu, "Optically transparent coding metasurface with simultaneously low infrared emissivity and microwave scattering reduction," Opt. Express **28**(19), 27774–27784 (2020).
36. F. Yuan, G. -M. Wang, H. -X. Xu, T. Cai, X. -J. Zou, and Z. -H. Pang, "Broadband RCS Reduction Based on Spiral-Coded Metasurface," Antennas Wirel. Propag. Lett. **16**, 3188–3191 (2017).
37. L. Qiu, G. Xiao, X. Kong, *et al.*, "Broadband, polarization insensitive low-scattering metasurface based on lossy Pancharatnam-Berry phase particles," Opt. Express **27**(15), 21226 (2019).
38. J. C. I. Galarregui, A. T. Pereda, J. L. M. de Falcón, *et al.*, "Broadband radar cross-section reduction using AMC technology," IEEE Trans. Antennas Propagat. **61**(12), 6136–6143 (2013).
39. X. Han, H. Xu, Y. Chang, M. Lin, Z. Wenyuan, X. Wu, and X. Wei, "Multiple diffuse coding metasurface of independent polarization for RCS reduction," IEEE Access **8**, 162313–162321 (2020).
40. M. K. T. Al-Nuaimi, W. Hong, and W. G. Whittow, "Aperiodic Sunflower-Like Metasurface for Diffusive Scattering and RCS Reduction," Antennas Wirel. Propag. Lett. **19**(7), 1048–1052 (2020).
41. C. Fu, X. Zhang, X. Liu, *et al.*, "RCS reduction of composite transparent flexible coding metasurface combined phase cancellation and absorption," Opt. Express **31**(17), 27365–27380 (2023).
42. Y. Zhou, X. Cao, J. Gao, H. Yang, and S. Li, "Reconfigurable metasurface for multiple functions: magnitude, polarization and phase modulation," Opt. Express **26**(22), 29451 (2018).
43. Y. Pang, Y. Li, J. Wang, M. B. Yan, S. Qu, S. Xia, and Z. Xu, "Electromagnetic reflection reduction of carbon composite materials mediated by collaborative mechanisms," Carbon **147**, 112–119 (2019).
44. M. K. T. Al-Nuaimi, S. -L. Zhu, W. G. Whittow, R. -S. Chen, G. -L. Huang, and A. Mahmoud, "Design of Alvarez Beam Scanning Reflectarray with Inversely Proportional Focal Length," Antennas Wirel. Propag. Lett. **22**(6), 1416–1420 (2023).
45. D. Wang, K. Liu, X. Li, G. Wang, S. Tang, and T. Cai, "Bifunctional spoof surface plasmon polariton meta-coupler using anisotropic transmissive metasurface," Nanophotonics **11**(6), 1177–1185 (2022).
46. X. Cui, D. Liu, Z. Dan, D. Wang, B. Wang, G. Wu, B. Wang, T. Zheng, and Cai, "Wideband and high-efficiency spin-locked achromatic meta-device," Nanophotonics **12**(1), 119–127 (2023).
47. M. K. T. Al-Nuaimi and W. G. Whittow, "Design of QR-Coded Metasurfaces for RCS Reduction at mmWave," IEEE Access **10**, 66267–66272 (2022).
48. T. Han, K. Wen, Z. Xie, *et al.*, "An Ultra-Thin Wideband Reflection Reduction Metasurface Based on Polarization Conversion," Progress In Electromagnetics Research **173**, 1–8 (2022).
49. T. Cai, B. Zheng, J. Lou, *et al.*, "Experimental Realization of a Superdispersion-Enabled Ultrabroadband Terahertz Cloak," Adv. Mater. **34**(38), 2205053 (2022).
50. M. K. T. Al-Nuaimi, "Design of Polarization-Insensitive and Angularly Stable Metasurfaces with Symmetric Cubic Phase Distribution for Broadband RCS Reduction," *IEEE Trans. Antennas Propagat.*, early access 2023.
51. X. Wang, X Wang, H. Ren, *et al.*, "Optically Transparent Microwave Shielding Hybrid Film Composited by Metal Mesh and Graphene," Progress in Electromagnetics Research **170**, 187–197 (2021).
52. M. K. T. Al-Nuaimi, W. Hong, and W. G. Whittow, "Nature-inspired orbital angular momentum beam generator using aperiodic metasurface," J. Phys. D: Appl. Phys. **54**(27), 275106 (2021).
53. F. Ding, "A Review of Multifunctional Optical Gap-Surface Plasmon Metasurfaces," Progress In Electromagnetics Research **174**, 55–73 (2022).